Evaluating Vertical Velocity Retrievals from Vertical Vorticity Equation Constrained Dual-Doppler Analysis of Real, Rapid-Scan Radar Data

Joshua G. Gebauer,[a,b] Alan Shapiro,[a] Corey K. Potvin,[a,c] Nathan A. Dahl,[d,e] Michael I. Biggerstaff,[a,d] and A. Addison Alford[d]

[a] School of Meteorology, University of Oklahoma, Norman, Oklahoma
[b] Earth Observing Laboratory, National Center for Atmospheric Research, Boulder, Colorado
[c] NOAA/OAR/National Severe Storms Laboratory, Norman, Oklahoma
[d] Cooperative Institute for Severe and High-Impact Weather Research and Operations, Norman, Oklahoma
[e] NOAA/NWS/Storm Prediction Center, Norman, Oklahoma

ABSTRACT: Accurate vertical velocity retrieval from dual-Doppler analysis (DDA) is a long-standing problem of radar meteorology. Typical radar scanning strategies poorly observe the vertical component of motion, leading to large uncertainty in vertical velocity estimates. Using a vertical vorticity equation constraint in addition to a mass conservation constraint in DDA has shown promise in improving vertical velocity retrievals. However, observation system simulation experiments (OSSEs) suggest this technique requires rapid radar volume scans to realize the improvements due to the vorticity tendency term in the vertical vorticity constraint. Here, the vertical vorticity constraint DDA is tested with real, rapid-scan radar data to validate prior OSSEs results. Generally, the vertical vorticity constraint DDA produced more accurate vertical velocities from DDAs than those that did not use the constraint. When the time between volume scans was greater than 30 s, the vertical velocity accuracy was significantly affected by the vorticity tendency estimation method. A technique that uses advection correction on provisional DDA wind fields to shorten the discretization interval for the vorticity tendency calculation improved the vertical velocity retrievals for longer times between volume scans. The skill of these DDAs was similar to those using a shorter time between volume scans. These improvements were due to increased accuracy of the vertical vorticity tendency using the advection correction technique. The real radar data tests also revealed that the vertical vorticity constraint DDAs are more forgiving to radar data errors. These results suggest that vertical vorticity constraint DDA with rapid-scan radars should be prioritized for kinematic analyses.

KEYWORDS: Vorticity; Radars/Radar observations; Variational analysis

1. Introduction

Dual-Doppler analysis (DDA) has been used as a technique to retrieve three-dimensional wind fields from radial velocity observations from two radars for over 60 years. These wind retrievals provided critical insight into mesoscale phenomena such as ordinary convection (Mahoney 1988), lightning (Lang and Rutledge 2002), squall lines (Biggerstaff and Houze 1993; Conrad and Knupp 2019), supercells (Brandes et al. 1988; Kosiba et al. 2013; Betten et al. 2018), and hurricanes (Kosiba and Wurman 2014; Alford et al. 2019). DDA typically retrieves the wind field using mass conservation and radial velocity observations from two radars as constraints. With adequate radar cross-beam angles, DDA can obtain the horizontal wind components with sufficient accuracy for kinematic analysis, but errors in the retrieved vertical velocity can be large (Doviak et al. 1976; Ray and Wagner 1976; Nelson and Brown 1987; Matejka and Bartels 1998; Potvin et al. 2012a). The vertical component of motion is poorly sampled by typical radar-scanning strategies due to the shallow elevation angles that are used. This means retrieved vertical velocity from DDA strongly depends on the mass conservation constraint. Errors in the horizontal divergence accumulate

with height when integrating the mass conservation equation upward, resulting in vertical velocity retrievals degrading with height (Ray et al. 1980). Vertical velocity errors can also come from boundary specification for the integration of the mass conservation equation. The impermeability condition ($w = 0$ on a flat surface) is the simplest boundary condition to impose; however, radar datasets often do not have data extending to the ground due to scan geometry, ground clutter, and Earth's curvature. In such cases, large errors may occur if a significant portion of the low-level horizontal wind divergence is missing.

Various DDA techniques and methods have been developed to mitigate errors in vertical velocity retrievals. Brandes (1977) set the horizontal divergence in the data void to some fraction of the divergence at the lowest level with data. This fraction, however, is arbitrary and the divergence at the lowest data level may not be representative of the divergence in the data void. Another technique is to set vertical velocity to zero at the storm top and integrate downward. Ray et al. (1980) show theoretically that downward integration of the anelastic mass conservation equation accumulates less error than upward integration due to density decreasing with height, but they also state this benefit may be counteracted if the upper boundary condition is inaccurate. This is often the case as radar scans often do not reach storm top, and even if they do, the assumption that vertical velocity is zero there

Corresponding author: Joshua G. Gebauer, joshua.gebauer@ou.edu

may be invalid. Other techniques set an upper and lower boundary condition when solving for vertical velocity (O'Brien 1970; Ray et al. 1980; Protat and Zawadzki 1999). These techniques can be more successful than upward or downward integration alone, but issues with boundary condition specification remain.

A different class of DDA obtains the wind field using a variational approach (Gao et al. 1999; Shapiro et al. 2009). In these retrievals, observation and mass conservation constraints serve as weak constraints applied in a least squares error sense (Sasaki 1970). As the mass conservation equation is not explicitly integrated in this type of DDA, vertically compounding errors and boundary-condition-specification errors are mitigated. Observation simulation system experiments (OSSEs) show that variational DDA techniques have better vertical velocity retrievals than DDAs requiring integration of the mass conservation equation (Potvin et al. 2012a). Another benefit of the weak-constraint variational approach is that nontypical retrieval constraints are easier to implement since the constraint does not have to be fully realized. An example would be the vertical vorticity equation, which has been used to improve vertical velocity retrievals (Shapiro et al. 2009). The vertical vorticity equation, like the mass conservation equation, connects vertical velocity to the horizontal wind field. Studies using a vertical vorticity equation constraint in their DDAs found the constraint can improve vertical velocity retrievals over DDA approaches not including the constraint, though there are some difficulties (Potvin et al. 2012b; Dahl et al. 2019). The main difficulty is the required estimation of the vertical vorticity tendency term. This term must be estimated using consecutive radar volume scans, so when the time between radar volume scans is long, the vertical vorticity constraint can significantly degrade the DDA wind fields. However, in OSSEs it was found that the vertical vorticity constraint can improve vertical velocity retrievals in high-resolution when volume scan times are short (~30 s) or in cases with missing low-level data (Potvin et al. 2012b; Dahl et al. 2019). Due to radar scanning limitations, these OSSE results have not been previously verified using real, rapid-scan radar data, but advancements and proliferation of rapid-scan radars has now made it possible to conduct such tests. This study uses data from two rapid-scan mobile radars to evaluate vertical velocity retrievals from DDA using a vertical vorticity equation constraint. A third mobile radar that was vertically pointing was used as the verification dataset. Section 2 describes the radars, data collection, and quality control. The DDA methodology and experiment is presented in section 3. The results are found in section 4, and the study is summarized in section 5.

2. Data collection and quality control

a. Data collection

Tests of the vertical vorticity constraint DDA were performed using volumes of data gathered at no more than 30-s intervals. Two radars from the Advanced Radar Research Center (ARRC)—the rapid-scanning, X-band polarimetric radar

(RaXPol; Pazmany et al. 2013) and the Atmospheric Imaging Radar (AIR; Isom et al. 2013; Kurdzo et al. 2017)—met this requirement and were used to collect the dual-Doppler dataset for this study. RaXPol is capable of collecting a 360° azimuth scan in 2 s. The AIR is an X-band radar that transmits a 20° × 1° beam and uses a 36-element array to collect 36 simultaneous channels of receive data (Kurdzo et al. 2017). In a postprocessing step, digital beamforming is performed to obtain twenty 1° × 1° beams in the vertical. Since the AIR obtains data in the vertical simultaneously, mechanical steering of the array in azimuth allows the radar to collect a 20° × 180° volume of data in as little as 9 s. One trade off of the AIR's unique design is that transmitting a fan-beam distributes the pulse power over a wider area, which limits the maximum range of the AIR to around 21 km due to signal loss. In addition to the rapid-scan radars, the Shared-Mobile Atmospheric Research and Teaching Polarimetric Radar 1 (SR1-P; Biggerstaff et al. 2005) was used as a DDA verification source. SR1-P, the newest in the series of mobile, C-band radars, was completed in 2018. As a C-band radar, SR1-P is less prone to attenuation, making it a good radar for verification.

Data were collected for this study on 4 September 2018. On this day, southerly flow throughout the depth of the troposphere in central Oklahoma (between a broad upper-level ridge to the east and a trough associated with the subtropical jet to the west) advected anomalously moist air into the region. Soundings from the National Weather Service site in Norman, Oklahoma, showed high precipitable water content suggestive of an almost tropical environment, along with considerable instability; the 1200 UTC sounding showed no CIN, and a CAPE value of 1068 J kg^{-1}, though peak instability in the afternoon was likely much greater. The winds throughout the depth of the troposphere were south to southwesterly at 20–30 kt (1 kt ≈ 0.51 m s^{-1}). The instability combined with minimal vertical wind shear and high precipitable water led to widespread ordinary convection over central Oklahoma. The storm targeted for analysis initiated around 2100 UTC near Chickasha, Oklahoma, and moved northward. For the next hour, this storm grew in size as it moved through the dual-Doppler domain. The storm began to dissipate around 2200 UTC at the northern edge of the dual-Doppler lobe.

The mobile radar positions during data collection are shown in Fig. 1. The AIR was positioned north of the target storm and RaXPol was located 15.48 km at 121.66° from the AIR. SR1-P was positioned in the dual-Doppler lobe, 12.35 and 14.76 km away from RaXPol and the AIR, respectively. RaXPol began data collection at 2055 UTC and continued scanning until 2159 UTC. The Nyquist velocity was 30.8 m s^{-1} and the maximum unambiguous range was 37.5 km. Each volume scan consisted of 360° plan position indicator (PPI) scans at 13 elevation angles from 1 to 19.5° every 1.5°. With this scanning strategy, RaXPol collected a full volume of data every 30 s. The AIR began data collection at 2120 UTC and ended at 2209 UTC. The AIR's Nyquist velocity was 25 m s^{-1} and the maximum unambiguous range was 47.12 km; however, as previously mentioned, the AIR typically only obtains returns out to about 21 km. The AIR performed 165° sector scans, obtaining a 20° × 165° volume of data every 9 s. In
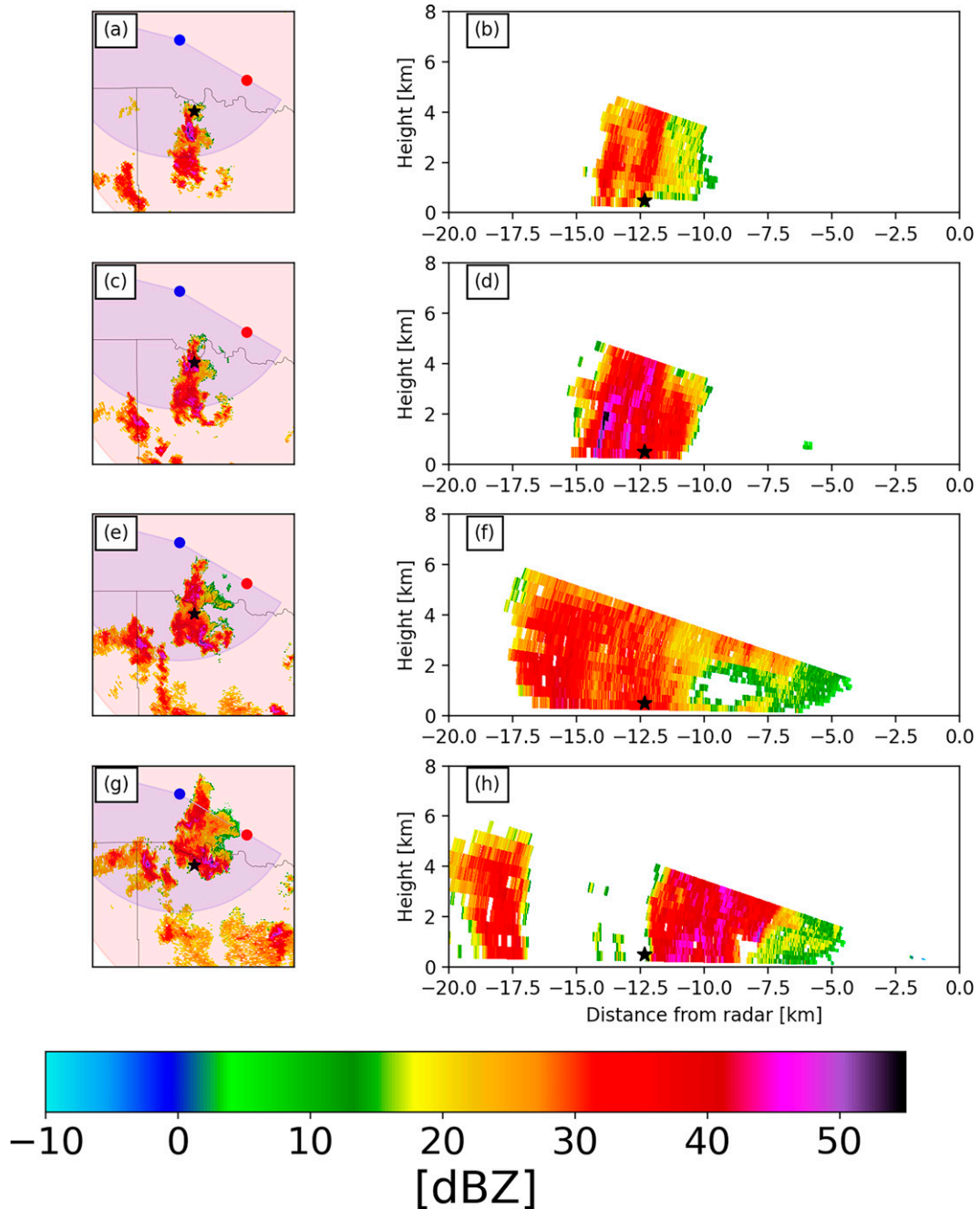
FIG. 1. Radar reflectivity (dBZ) from RaXPol at (a),(b) 2124:11, (c),(d) 2130:40, (e),(f) 2139:10, and (g),(h) 2148:10 UTC. PPIs at 3.5° are shown in (a), (c), (e), and (g) and vertical cross sections derived from PPI scans at 240.58° are shown in (b), (d), (f), and (h). RaXPol and the AIR were located at the red and blue circles, respectively. The position of SR1-P is represented by the black star. The area scanned by only RaXPol is shaded red and the area scanned by the AIR and RaXPol is shaded violet.

postprocessing the data were oversampled in elevation to 0.5° beam spacing. SR1-P served as the verification point for the vertical velocity retrievals, obtaining PPIs at 88° elevation every 18 s. While 90° PPIs would have been optimal, radar pedestal constraints limited the maximum elevation angle to 88°. Additionally, the SR1-P periodically performed a 2° PPI to

remove rainwater from the radar antenna, creating occasional gaps in the verification dataset. The SR1-P Nyquist velocity was 12.8 m s^{-1} the unambiguous range was 150 km. With the described radar placement and scanning strategies, dual-radar observations of the storm extended to 4.625 km above ground level over the SR1-P. This limits our study to the verification of

low-level vertical velocity, and likely the most intense vertical velocities, which typically occur at higher altitudes, are not retrieved at the SR1-P location. Despite this limitation, this unique dataset allows us to test using a vertical vorticity equation in DDAs for the first time with a real, rapid scan radar dataset. To our knowledge, the 4 September 2018 dataset is one of the most rapidly scanned dual-Doppler datasets ever collected.

b. Data quality control

The RaXPol data were quality controlled using the Solo3 software (Oye et al. 1995). This consisted of using Solo3's despeckling algorithm and then removing the remaining radar artifacts through manual editing. There were also azimuthal displacement errors in the RaXPol dataset, likely from an encoder issue. These displacements were sometimes large, often over 1°. Complicating matters, the azimuthal displacements were not constant within the same sweep. Due to this unique issue, an azimuthal displacement correction technique was created that leveraged retrieved pattern translation components from the Shapiro et al. (2010) spatially variable advection correction procedure to estimate azimuthal displacements. This technique is described in the appendix.

The full AIR dataset consisted of 14 220 sweeps, too many to manually edit. Therefore, the data were quality controlled using automated routines. In the initial postprocessing of the AIR data, a ground clutter filter was applied. This substantially reduced the ground clutter in the AIR dataset, but some remained. Ground clutter maps were created from the first few volume scans when there was little observable precipitation for the AIR. These clutter maps were then used to remove the remaining ground clutter throughout the entire dataset. The remaining speckles in the AIR dataset were removed with the following routine. An approximately 600 m × 600 m averaging region was centered on the radar bin being analyzed. Then five time levels centered on the time currently being quality controlled were considered. At each time level, it was determined if greater than 30% of the averaging region contained echoes. If fewer than three time levels had greater than 30% echo coverage, the radar bin being evaluated was considered a speckle and was removed. After despeckling, bad radial velocity bins were still present. To remove these, the same despeckling averaging region was used. Bins with radial velocity differing by more than 5 m s^{-1} from the region-averaged radial velocity were removed. This procedure was highly tailored to this particular dataset, and the thresholds used for this dataset would likely not be applicable for other datasets, especially in more vigorous convection.

The wind speeds associated with the target storm were not high (~10 m s^{-1}), and so neither the AIR nor RaXPol had aliased velocities. The SR1-P did have some velocity aliasing in the stronger downdrafts since it sampled the sum of particle terminal fall velocity and the air vertical velocity. This aliasing was easy identified as large positive vertical (i.e., upward) velocities should not coincide with falling precipitation (at least in this storm), so aliased velocities were identified by high

reflectivity and strong positive radial velocities. Additionally, a high-bias in the SR1-P reflectivities needed to be corrected so the reflectivities could be used to estimate terminal fall velocity. The Weather Surveillance Radar-1998 Doppler (WSR-88D; Crum and Alberty 1993; Crum et al. 1998) are subject to calibration standards, so the KTLX (the closest WSR-88D to the storm) radar reflectivity can be used as the benchmark reflectivity for correcting this bias. KTLX was 63.86 km at 89.64° from SR1-P, but data from KTLX were too coarse in elevation and time to be used for a direct comparison, so the KTLX reflectivities were first compared to the RaXPol reflectivities. There was very little difference between the KTLX and RaXPol reflectivities at common data times around the SR1-P location, suggesting that the RaXPol reflectivities were unbiased and unaffected by attenuation in the vicinity of the SR1-P. The RaXPol reflectivities were then compared to the SR1-P reflectivities to estimate and correct the SR1-P reflectivity bias. This reflectivity bias was estimated to be 13.59 dBZ.

3. DDA methods and experiment design

a. Description of vertical vorticity equation constrained DDA

1) DDA CONSTRAINTS

The vertical vorticity equation constrained DDA used for this study was developed by Shapiro et al. (2009) and modified by Potvin et al. (2012b) and Dahl et al. (2019). Only a brief overview of this variational procedure is presented here. In this procedure, observations, a mass conservation equation, a vertical vorticity equation, and spatial smoothness are imposed weak constraints on the three-dimensional wind field. Together, these constraints form the following cost function:

$$J = J_O + J_M + J_V + J_S, \qquad (1)$$

where J_O is the observational constraint, J_M is the mass conservation constraint, J_V is the vorticity constraint, and J_S is the smoothness constraint.

Specifically, the observation constraint is

$$J_O = \lambda_O \left[\sum_{\text{Cart}} (V_{r_1}^{\text{obs}} - V_{r_1}^a)^2 + \sum_{\text{Cart}} (V_{r_2}^{\text{obs}} - V_{r_2}^a)^2 \right], \qquad (2)$$

where $V_{r_1}^{\text{obs}}$ and $V_{r_2}^{\text{obs}}$ are the radial velocities from radar 1 and radar 2 and $V_{r_1}^a$ and $V_{r_2}^a$ are radial velocities calculated from the analysis wind field for radar 1 and radar 2. Since this study uses rapid-scan radar data and the largest volume scan time in the dataset is 30 s, no correction for the scan rate of the radar is made when calculating this penalty term. The product of a nondimensional constraint weight and normalization factor λ_O is defined as

$$\lambda_O = C_O \left\{ \left(\frac{1}{M_1 + M_2} \right) \left[\sum_{\text{Cart}} (V_{r_1}^{\text{obs}})^2 + \sum_{\text{Cart}} (V_{r_2}^{\text{obs}})^2 \right] \right\}^{-1}, \qquad (3)$$

where C_O is the nondimensional user-defined constraint weight and M_1 and M_2 are the number of radial wind observations from radar 1 and radar 2.

The anelastic mass conservation constraint is

$$J_M = \lambda_M \sum_{\text{Cart}} \left(\frac{\partial u^a}{\partial x} + \frac{\partial v^a}{\partial y} + \frac{\partial w^a}{\partial z} + \frac{w^a}{\rho} \frac{d\rho}{dz} \right)^2, \quad (4)$$

where u, v, w, are the x, y, and z wind components and ρ is density, determined by

$$\rho z = \rho_o \exp\left(-\frac{z}{H} \right). \quad (5)$$

For this application, the scale height of the atmosphere H is set to 10 km, and ρ_o, which is the density at $z = 0$, is 1 kg m^{-3}. The weighting parameter λ_M is defined two different ways depending on the available data. When no provisional wind analysis is available, the mass conservation term is normalized by the azimuthal gradients in radial velocity,

$$\lambda_M = C_M \left\{ \left(\frac{1}{M_1 + M_2} \right) \left[\sum_{\text{Cart}} \left(\frac{1}{r_1} \frac{\partial V_{r_1}^{\text{obs}}}{\partial \theta} \right)^2 + \sum_{\text{Cart}} \left(\frac{1}{r_2} \frac{\partial V_{r_2}^{\text{obs}}}{\partial \theta} \right)^2 \right] \right\}^{-1}, \quad (6)$$

where r_1 and r_2 are the distances of radars 1 and 2, θ is azimuth from the location of the observation, and C_M is the user selected nondimensional weighting parameter. When there is a provisional analysis available, the constraint is normalized with the horizontal divergence in the provisional analysis so

$$\lambda_M = C_M \left\{ \left(\frac{1}{N} \right) \left[\sum_{\text{Cart}} \left(\frac{\partial u^p}{\partial x} + \frac{\partial v^p}{\partial y} \right) \right]^2 \right\}^{-1}, \quad (7)$$

where N is the number of analysis points in the analysis grid domain and u^p and v^p are the provisional analysis x and y components of the wind. In this study, provisional analyses are initial DDAs that do not have a vorticity constraint and have unoptimized constraint weighting.

For the vorticity equation constraint, the anelastic form of the vertical vorticity equation with no mixing terms [Eq. (1.4)] is used:

$$J_V = \lambda_V \sum_{\text{Cart}} \left[\frac{\partial \zeta}{\partial t} + u^a \frac{\partial \zeta^a}{\partial x} + v^a \frac{\partial \zeta^a}{\partial y} + w^a \frac{\partial \zeta^a}{\partial z} \right. $$
$$\left. + \left(\frac{\partial v^a}{\partial z} \frac{\partial w^a}{\partial x} - \frac{\partial u^a}{\partial z} \frac{\partial w^a}{\partial y} \right) + \zeta^a \delta^a \right]^2, \quad (8)$$

where ζ is vertical vorticity, $\zeta = \partial v/\partial x - \partial u/\partial y$, and δ is horizontal divergence, $\delta = \partial u/\partial x + \partial v/\partial y$. As noted in Shapiro et al. (2009), although baroclinicity can be very important in mesoscale convective flows, the baroclinic vorticity generation term is much more important in the horizontal vorticity equation than in the vertical vorticity equation, and is not even present in the anelastic form of the vertical vorticity equation. The calculation of the vorticity tendency term $\partial \zeta/\partial t$ requires a provisional wind analysis. Therefore,

$$\lambda_V = C_V \left\{ \left(\frac{1}{N} \right) \left[\sum_{\text{Cart}} \left(\frac{\partial \zeta}{\partial t} + u^p \frac{\partial \zeta^p}{\partial x} + v^p \frac{\partial \zeta^p}{\partial y} + \zeta^p \delta^p \right)^2 \right] \right\}^{-1}, \quad (9)$$

where C_V is the user selected nondimensional weighting parameter.

Finally, the smoothness constraint is

$$J_S = \lambda_{S_1} \sum_{\text{Cart}} \left[\left(\frac{\partial^2 u^a}{\partial x^2} \right)^2 + \left(\frac{\partial^2 u^a}{\partial y^2} \right)^2 + \left(\frac{\partial^2 v^a}{\partial x^2} \right)^2 + \left(\frac{\partial^2 v^a}{\partial y^2} \right)^2 \right]$$
$$+ \lambda_{S_2} \sum_{\text{Cart}} \left[\left(\frac{\partial^2 u^a}{\partial z^2} \right)^2 + \left(\frac{\partial^2 v^a}{\partial z^2} \right)^2 \right] + \lambda_{S_3} \sum_{\text{Cart}} \left[\left(\frac{\partial^2 w^a}{\partial x^2} \right)^2 + \left(\frac{\partial^2 w^a}{\partial y^2} \right)^2 \right]$$
$$+ \lambda_{S_4} \sum_{\text{Cart}} \left(\frac{\partial^2 w}{\partial z^2} \right)^2. \quad (10)$$

As in Potvin et al. (2012b) and Dahl et al. (2019), all DDAs were calculated with $\lambda_{S_1} = \lambda_{S_2} = \lambda_{S_3} = \lambda_{S_4} = \lambda_S$. As with the mass conservation constraint, the nondimensionalization for this constraint depends on whether a provisional analysis available, so

$$\lambda_S = C_S \left\{ \left(\frac{1}{M_1 + M_2} \right) \left[\sum_{\text{Cart}} \left(\frac{1}{r_1} \frac{\partial^2 V_{r_1}^{\text{obs}}}{\partial \theta^2} \right)^2 + \sum_{\text{Cart}} \left(\frac{1}{r_2} \frac{\partial^2 V_{r_2}^{\text{obs}}}{\partial \theta^2} \right)^2 \right] \right\}^{-1}, \quad (11)$$

if there is no provisional analysis and

$$\lambda_S = C_S \left\{ \left(\frac{1}{N} \right) \sum_{\text{Cart}} \left[\left(\frac{\partial^2 u^p}{\partial x^2} \right)^2 + \left(\frac{\partial^2 u^p}{\partial y^2} \right)^2 + \left(\frac{\partial^2 u^p}{\partial z^2} \right)^2 \right. \right.$$
$$\left. \left. + \left(\frac{\partial^2 v^p}{\partial x^2} \right)^2 + \left(\frac{\partial^2 v^p}{\partial y^2} \right)^2 + \left(\frac{\partial^2 v^p}{\partial z^2} \right)^2 \right] \right\}^{-1}, \quad (12)$$

if a provisional analysis is available, where C_S is a user selected nondimensional weighting parameter.

One may notice that (7), (9), and (12) do not include w in the normalization factors. The potential for large errors in w in the provisional retrievals (which is the problem the vorticity constraint DDA is used to mitigate) precludes the use of w in the normalization. The normalization factors are included in the constraints to reduce tuning required for the constraints' nondimensional weights. However, even with normalization, tuning can be necessary to obtain the most accurate DDAs. For this study, $C_O = 1$, $C_M = 0.001$, and $C_S = 0.0001$ were used for all provisional DDAs (there is no vorticity equation constraint in the provisional DDAs so C_V is not applicable), and $C_O = 1$, $C_M = 0.3$, $C_V = 0.1$, and $C_S = 0.0001$ for the analysis DDA runs. For final DDAs that do not use the vorticity equation constraint, the values of C_O, C_M, and C_S remain the same as those with the vorticity constraint. The values chosen for the provisional DDA were the same as those used in Dahl et al. (2019), since these values produced good provisional retrievals. The weights for the final DDA were modified from those used in Dahl et al. (2019) as

the vorticity equation constraint required more weight in order to affect the wind retrievals in the current case.

2) VORTICITY TENDENCY CALCULATION

The calculation of the vorticity tendency underpins the need for rapid-scan radar for DDAs that use the vertical vorticity constraint. Wind fields from consecutive analysis times are needed to calculate this time-tendency term. Potvin et al. (2012b) and Dahl et al. (2019) used consecutive provisional DDAs for the vorticity tendency calculation. Provisional DDAs can be used for this calculation as the u and v components in even basic DDAs techniques are well constrained by the observations. Even with accurate provisional retrievals, however, when the time between two provisional analyses is large, discretization errors in the vorticity tendency increase, degrading the performance of the DDA.

The calculation of the vorticity tendency occurs outside of the DDA retrieval and the field is included as input for the DDA program. Therefore, the vorticity tendency remains constant throughout the minimization of (1). Tests are conducted using three different vorticity tendency calculations. The first is a simple centered difference of the vorticity fields from provisional retrievals from the volume scans directly before and after the analysis time so that

$$\frac{\partial \zeta}{\partial t}(x, t^a) = \frac{\zeta^p(x, t^a + \tau) - \zeta^p(x, t^a - \tau)}{2\tau}, \qquad (13)$$

where τ is the time between volume scans (referred to as a "brute force" approach). This technique is most susceptible to discretization error when τ becomes large, but Dahl et al. (2019) found that when τ is sufficiently small (~10–30 s) (13) provides estimates of the vorticity tendency that are accurate enough to improve vertical velocity retrievals over DDAs that do not include a vorticity constraint. However, the vertical velocity retrievals became significantly degraded when τ exceed 30 s.

The second method is the u and v advection correction method first used by Dahl et al. (2019). In this method, the Shapiro et al. (2010) two-dimensional (2D) advection correction procedure is applied to the u and v fields from the provisional retrievals to shorten the discretization interval of the centered difference of the provisional vorticity fields so that

$$\frac{\partial \zeta}{\partial t}(x, t^a) = \frac{\zeta(x, t^a + \Delta t) - \zeta(x, t^a - \Delta t)}{2\Delta t}, \qquad (14)$$

where Δt is the computational time step used in the advection correction procedure. Dahl et al. (2019) found this method produced the most consistent DDA vertical velocity results as it had less degradation of the w field with increasing volume scan time. However, when τ was increased to 150 s, this method still produced less accurate w fields than DDAs that did not use the vorticity equation constraint. Since this method uses two-dimensional advection correction, the advection correction is conducted separately on each level in the analysis domain. This has the potential to create vertical discontinuities in the calculated vorticity tendency. These errors

would be exacerbated with larger τ as smaller changes in the pattern translation components can lead to larger horizontal displacement error than when τ is small.

The third method uses a three-dimensional (3D) advection correction procedure similar to the 2D procedure (Gebauer 2020). This procedure has not been used to calculate the vorticity tendency, but since the whole analysis volume is corrected at once it should not be subject to the discontinuity errors that can occur with the 2D technique. One downside of using the 3D advection correction technique is the additional data loss at the top and bottom of the data coverage area leads to the vorticity constraint being applied at fewer locations, as the constraint can only be applied where the vorticity tendency can be estimated.

3) RETRIEVAL PROCEDURE

The variational dual-Doppler procedure begins with the gridding of the RaXPol and AIR data with a Cressman filter (Cressman 1959). For this study, the dual-Doppler analysis was conducted at 125-m resolution in all dimensions and a 400-m Cressman radius was used. After the RaXPol and AIR data are gridded, a two-pass Leise filter (Leise 1982) is applied. This technique was found to produce more accurate gridded datasets than using a larger Cressman radius (Dahl et al. 2019). Provisional DDAs were conducted in a 30 km × 30 km × 7 km domain, but the final analyses were conducted in a 25 km × 25 km × 7 km domain (Fig. 2). The reduced horizontal extent in the analysis domain is due to data loss at the edges of the domain when advection correction is used to calculate the vorticity tendency. After application of the Leise filter, provisional DDAs with no vorticity equation constraint are conducted. If the final dual-Doppler retrieval does not contain a vorticity equation constraint (i.e., running the variational procedure described above with $C_v = 0$) then the provisional retrieval is only performed for the analysis time. This provisional retrieval is used to calculate the normalization factor for the mass conservation constraint. If a vorticity equation constraint is applied, provisional retrievals are conducted for the analysis time t^a and also for the $t - \tau$ and $t + \tau$ times. These provisional retrievals are used for the vorticity tendency calculation, and the analysis time provisional retrieval is also used to calculate the normalization factors for the mass conservation and vertical vorticity constraints. Once the provisional retrievals are obtained and the vorticity tendency is calculated using one of the three methods described above, the final analysis time DDA is performed. Since this is a variational retrieval, the procedure obtains winds for the entire analysis domain, including regions where there are no radar data. However, only regions with data from both radars and cross-beam angles greater than 15° are considered in the final analyses.

b. Experiment design

1) REFERENCE DDAs

Since this study aims to determine if the vorticity equation constrained DDA improves estimates of the vertical velocity field, reference retrievals that do not use the vorticity equation
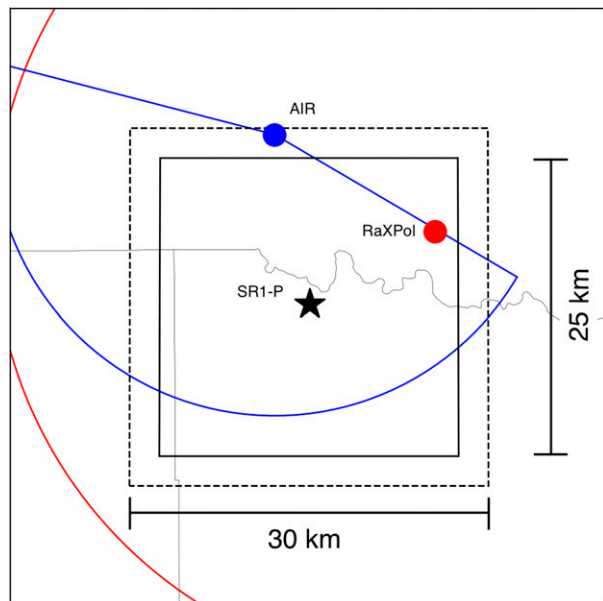
FIG. 2. Provisional DDA domain (dashed border) and final analysis DDA domain (solid border). The location and scanning area of the AIR is shown in blue and the location and scanning area of RaXPol is in red. The black star is the location of SR1-P.

constraint are needed for comparison. Two different techniques are used as a reference. The first is the previously described variational DDA with no vertical vorticity constraint. The second is a "traditional" DDA that directly integrates the anelastic mass conservation equation with the divergence in the data void set to a fraction of the divergence at the lowest level with data (Brandes 1977). Specifically, the traditional DDA used here is the same as Dahl et al. (2019). The divergence in the data void is set to 0.8 times the divergence at the lowest level; however, due to the storm's proximity to the radars in this particular dataset, the low-level data voids are minimal and this parameter does not have a significant effect on the retrievals.

2) VORTICITY EQUATION CONSTRAINED DDAs

Based on the previous OSSEs (Dahl et al. 2019), the rapid-volume scans of the AIR and RaXPol are ideal for using the

vorticity constraint DDA, but it is also important to evaluate how the DDA performs with longer times between volume scans when real data are used. One can test the impact of the time between volume scans on the DDA by varying τ for the calculation of the vorticity tendency from the provisional retrievals. For example, vorticity constraint DDAs with 90 s between volume scans can be tested by calculating the vorticity tendency from the provisional retrievals 90 s before and after the analysis time. It is important to note these results will not include advection errors that would occur with longer volume scan times since the true volume scan time for the data that were used for the provisional DDAs is still 30 s for RaXPol and 9 s for the AIR.

The vorticity constraint DDAs were performed for τ of 30, 90, and 150 s using each of the three methods for calculating the vorticity tendency described in section 3a(3). The DDAs were run using the 4 September 2018 dataset from 2121:11 to 2148:10 UTC. A summary of the 11 DDA experiments and their names is shown in Table 1.

3) VERIFICATION

In DDA OSSEs, the verification is often restricted to comparing the retrieved wind field to the simulated wind field used to generate the emulated radar observations ("truth"). Unfortunately, the use of real-radar data for this study makes the verification of the DDAs more complicated as the "truth" has to come from observations. It is particularly challenging to verify w as observations of vertical motion are uncommon and when they are available, they often only provide a profile at a single location. The only observations available for verification of w for this study come from the SR1-P. Since there is only one verification source for w, the verification of the DDAs is conducted over multiple scans to assess the performance of the retrieval for different sections of the storm as it passes over the SR1-P. Since the scan geometry for the verification point is static, it is impossible to assess how retrieval performance varies with cross-beam angle and vertical data availability.

The use of a vertically pointing radar as a verification source has its own difficulties. The SR1-P, with a beamwidth of 1.5°, has a smaller effective horizontal resolution than the DDAs. This could potentially be a source of differences

TABLE 1. Names and descriptions of the dual-Doppler experiments performed for this study.

| Name	Variational technique?	Vorticity constraint?	Vorticity tendency calculation	Time between volume scans (s)
TRAD	No	No	—	—
NOVORT	Yes	No	—	—
30s_BF	Yes	Yes	Brute force	30
90s_BF	Yes	Yes	Brute force	90
150s_BF	Yes	Yes	Brute force	150
30s_2dADV	Yes	Yes	2D ADV correction	30
90s_2dADV	Yes	Yes	2D ADV correction	90
150s_2dADV	Yes	Yes	2D ADV correction	150
30s_3dADV	Yes	Yes	3D ADV correction	30
90s_3dADV	Yes	Yes	3D ADV correction	90
150s_3dADV	Yes	Yes	3D ADV correction	150
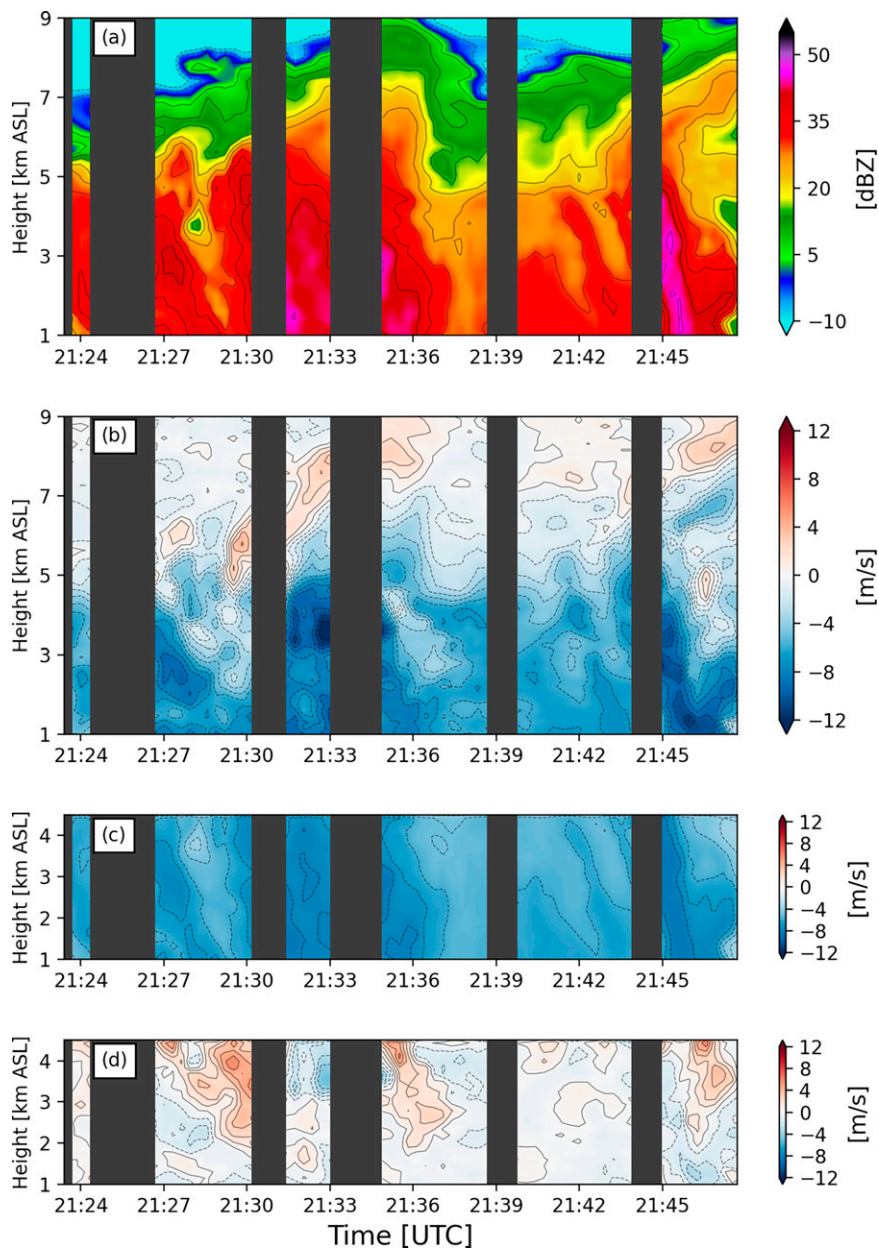
FIG. 3. SR1-P (a) reflectivity, (b) dealiased radial velocities, (c) terminal fall velocity calculated from (15) using the bias corrected SR1-P reflectivity, and (d) resulting observed vertical velocities after the terminal fall velocity was removed from the radial velocities. For (a) the contour interval is 5 dBZ and for (b), (c), and (d) the contour interval is 1 m s^{-1} with negative values shown with dashed contours. SR1-P was located 405 m MSL.

between the retrieved and observed vertical velocities, especially if there is a tight horizontal gradient in the vertical velocity as that location. Additionally, the SR1-P was not completely vertically pointing (88° PPI instead of 90° tilt) so the radial velocities have a small contribution from the horizontal wind components. To mitigate these potential biases, the radial velocities from the entire 18-s PPI are averaged to reduce the influence from the horizontal wind components

and to make the effective resolution of the measurements closer to that of the DDAs. The terminal fall velocity must be removed from the radial velocities in order to use the SR1-P as verification for w. The terminal velocity w_t (Fig. 3) is obtained using an empirical relationship from Atlas et al. (1973),

$$w_t = aZ^b\left(\frac{\rho_o}{\rho}\right)^{0.4},\qquad(15)$$
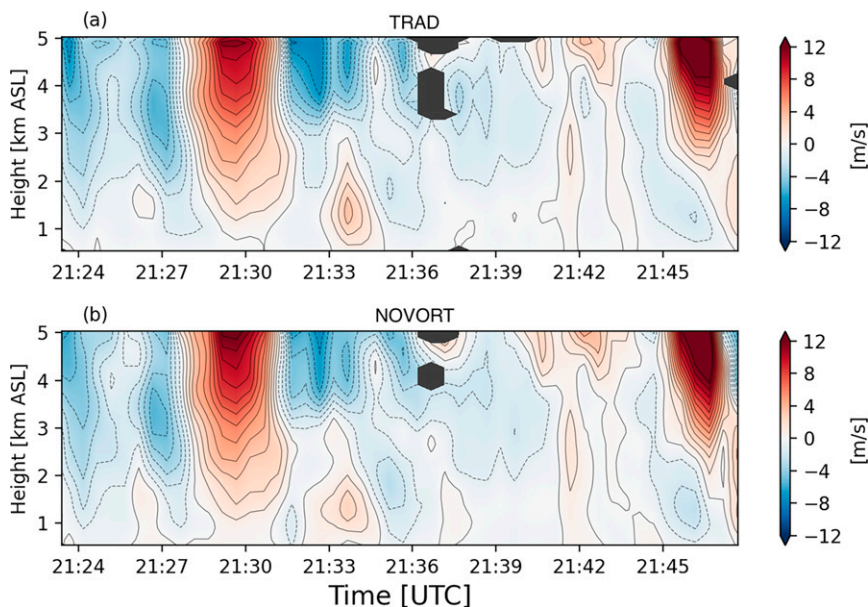
FIG. 4. Vertical velocities retrieved by the (a) TRAD and (b) NOVORT DDAs at the SR1-P verification column for the entire DDA time period. The black contour interval is 1 m s^{-1} with negative values shown with dashed contours. Areas shaded in gray are locations where no vertical velocity retrieval could be performed due to lack of data from one or both input radars.

with $a = -2.65$ and $b = 0.114$, where w_t is in m s^{-1} and Z is reflectivity in mm^6 m^{-3}. The relationship is meant for liquid drops and is not applicable at the melting level due to bright banding or above the freezing level for frozen precipitation, so the SR1-P data will only be used for verification below 4.5 km MSL, approximately 300 m below the freezing level. Dual-radar coverage only extends to 5 km at this location, so 500 m of DDA vertical velocities is unable to be quantitatively verified due to this restriction. Using (15) to estimate w_t introduces uncertainty into the w observations as (15) is only accurate to within 1 m s^{-1} for reflectivity less than 40 dBZ (Atlas et al. 1973). The increased uncertainty is due to the wide range of rain drop size distributions producing low reflectivity, from a large number of small drops (e.g., drizzle) to a small number of large drops at the edge of a convective storm. There is also uncertainty in the SR1-P reflectivity due to the bias described in section 2b. For all of these reasons, verification of the w retrievals at the SR1-P location focuses on the statistics plotted in Taylor diagrams (Taylor 2001). A Taylor diagram uses the relationship between centered root-mean-square error (CRMSE), correlation coefficient, and standard deviation to show them on one image. Since the mean of the data is irrelevant in these metrics, they are unaffected by a systematic bias in the observed w data from the terminal fall velocity calculation. The choice of terminal fall speed calculation could still affect the Taylor diagram statistics due to the nonlinear relationship between reflectivity and terminal fall speed, but such effects were found to be negligible in experiments with other terminal fall speed relationships as CRMSEs only varied 0.02 m s^{-1} (not shown).

These statistics were calculated at the SR1-P verification column for the entirety of each DDA experiment. The SR1-P

data were linearly interpolated to the same time–height grid used in the DDA. Times and heights that had no w estimate in any one of the DDA experiments were not included in the calculations of these statistics for any of the DDAs (0.8% of the time–height verification points). This was done so no experiment was rewarded or penalized for performing a w retrieval where another experiment could not.

4. Results

a. Qualitative verification at SR1-P location

The TRAD and NOVORT DDA w are very similar to each other at the SR1-P verification point (Fig. 4). This is not surprising since there is a minimal data gap near the ground in this dataset, so the variational approach does not gain much of an advantage over the traditional approach. Both DDAs retrieve updrafts at 2130 and 2147 UTC. The SR1-P verification w also depicts updrafts at these times; however, they are much weaker than the updrafts retrieved by the TRAD and NOVORT DDA. The TRAD and NOVORT DDAs also do not resolve the updraft at 2136 UTC, but at that time the verification column is at the edge of the detected radar echoes from the mobile radars, which is expected to degrade the retrieval. The TRAD and NOVORT DDAs are not adept at resolving the structure of the vertical motion. For example, near 2130 UTC, the SR1-P observed an updraft that was either tilted or descending with time, while DDA retrieved a more vertically oriented updraft with constant depth.

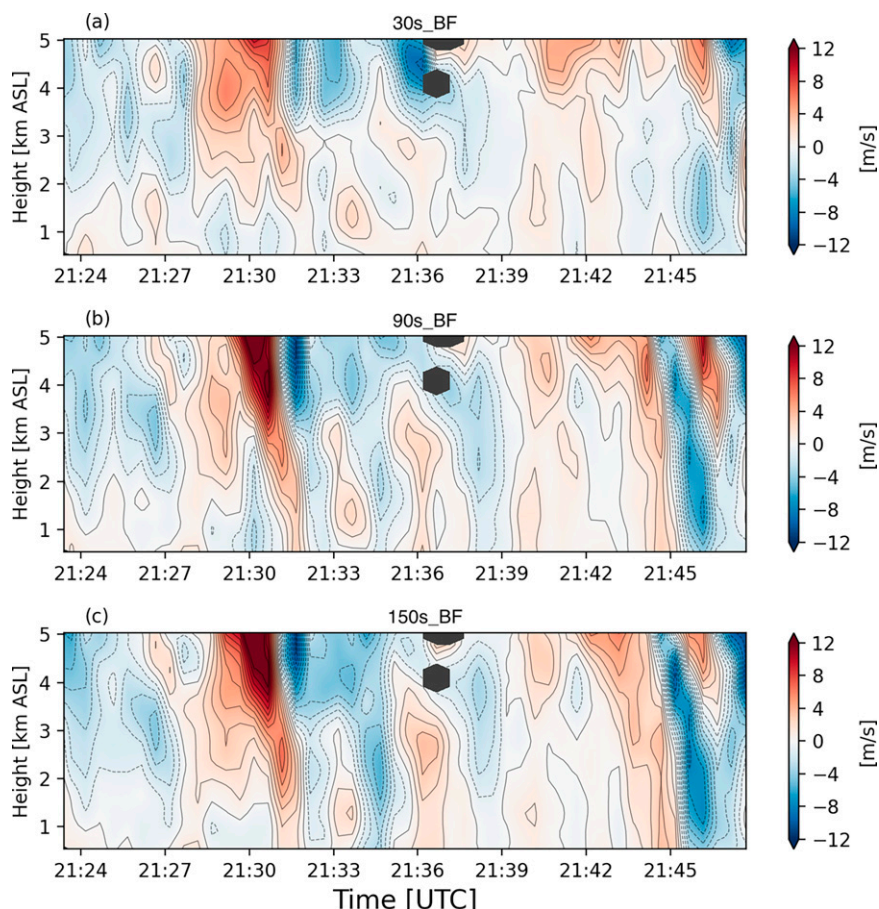The amplitudes of the updrafts retrieved with the 30s_BF DDA are closer to the SR1-P observations and the vertical

FIG. 5. As in Fig. 4, but for the (a) 30s_BF, (b) 90s_BF, and 150s_BF DDAs.

velocities also have more detail than those retrieved with the TRAD and NOVORT DDAs (Fig. 5a). One troubling detail in the 30s_BF results is the 2136 UTC large amplitude downdraft occurring above 3 km. The SR1-P observes an updraft at this time and location so this downdraft is a large error. This observed updraft is the same feature that the TRAD and NOVORT DDAs both were unable to correctly retrieve, likely from the proximity to the edge of data. The proximity to the edge of data is particularly important with the vorticity constraint DDAs as regions close to data voids may not have estimates of the vorticity tendency due to missing data. Without vorticity tendency, the vorticity constraint cannot be used at such locations. Indeed, it was found that no vorticity constraint is applied to the points above 3 km at 2136 UTC for vorticity constraint DDAs. The constraint is also not applied to points above 3 km at the end of the DDA period (after 2147 UTC) for similar reasons.

The 90s_BF and 150s_BF experiments highlight how longer volume scan times can degrade w retrievals when using a vorticity constraint (Figs. 5b,c). Large amplitude updrafts are retrieved after 2130 UTC with large amplitude downdrafts afterward. The vertical velocities after 2142 UTC also deviate from those observed by the SR1-P. Interestingly, although the 90s_BF and 150s_BF DDAs generally perform worse than

the 30s_BF DDAs, there are a few times where they perform better than the 30s_BF DDA. The 90s_BF and 150s_BF DDAs are particularly skillful at retrieving the small downdraft feature surrounded by updraft after 2127 UTC, and they do not have the large amplitude downdraft around 2136 UTC. This shows the uncertainty with using the brute force technique for calculating the vorticity tendency with longer times between volume scans.

When the 2D advection correction method is used for calculating the vorticity tendency with 90 s between volume scans, the high-amplitude updrafts and downdrafts that were present in the 90s_BF are no longer present and the w structures are much improved (Fig. 6b). The region above 3 km at 2136 UTC has the incorrect downdraft in all 2DADV DDAs. The proximity to the edge of the data is a larger issue when using advection correction because the procedure can result in loss of data at the edges of the data coverage area. The updraft at 2147 UTC is too weak in all 2D advection correction DDAs. On the other hand, the structure of the retrieved updraft at 2130 UTC is impressive when 2D advection correction is used, especially in the 90s_2DADV DDA. The 2D advection correction technique for the vorticity tendency calculation was not able to correct the strong updraft–downdraft pair in the 150-s DDA between 2130 and 2133 UTC (Fig. 6c),
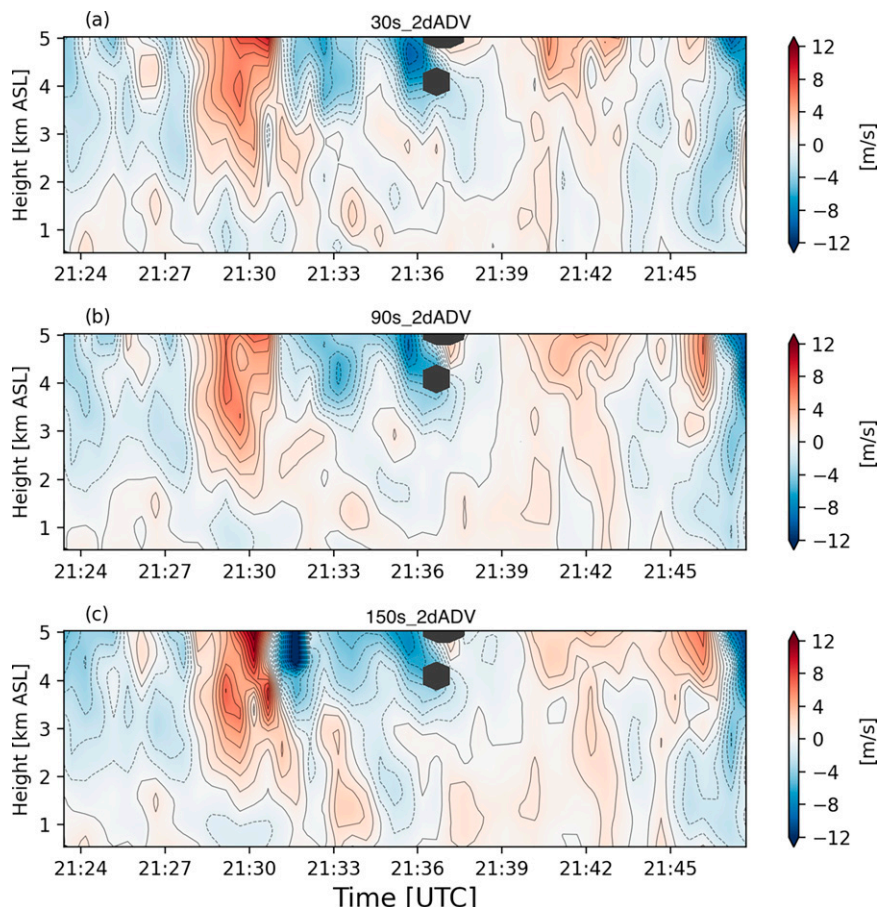
FIG. 6. As in Fig. 4, but for the (a) 30s_2DADV, (b) 90s_2DADV, and 150s_2DADV DDAs.

suggesting the 2D advection correction technique is still not providing an accurate enough estimate of the vorticity tendency.

Using the 3D advection correction technique for calculating the vorticity tendency does not result in large changes in the *w* at the verification column in the 30s_3DADV and 90s_3DADV DDAs (Figs. 7a,b). It does, however, improve the 150 s volume scan DDA as the large amplitude updraft–downdraft pair is no longer present and the retrieved *w* looks similar to that in the 90s_3DADV DDA (Fig. 7c).

b. Objective verification at the SR1-P location

The TRAD and NOVORT experiments had the largest CRMSE out of all of the DDAs experiments (Fig. 8). Interestingly, TRAD and NOVORT also had the highest correlation coefficient, but the CRMSE is high because the standard deviation of the retrieved *w* was much larger than the SR1-P observed standard deviation. This indicates the main errors in the TRAD and NOVORT DDAs are due to inflated amplitudes of the retrieved *w*. The 30s_BF DDA has a lower CRMSE than the TRAD and NOVORT DDAs. This reduction in CRMSE is mostly due to improvements in the amplitude of *w* as the standard deviation is closer to the observation standard deviation, but the correlation coefficient is lower

than the TRAD and NOVORT DDAs. The lower correlation coefficient is mostly due to the downdraft above 3 km at 2136 UTC (Figs. 5, 6, 7). The 90s_BF and 150s_BF have a larger CRMSE then the other vorticity constraint DDA experiments. Even so, the verification statistics for the 90s_BF and 150s_BF likely overestimate the skill of those retrievals as the large amplitude updrafts after 2130 UTC are not included in this verification due to missing SR1-P data. When advection correction is used for calculating the vorticity tendency, the 90- and 150-s DDAs have verification statistics similar to the 30s_BF DDA. The 90s_3DADV and 150s_3DADV DDAs have slight improvements in CRMSE over the 90s_2DADV and 150s_2DADV DDAs, respectively, but these improvements are smaller than the improvements of retrievals with that use 2D advection correction over those without advection correction. Using advection correction for the 30-s volume scan experiments resulted in the CRMSE slightly increasing, suggesting advection correction for 30 s between volumes scans for this case is unnecessary and can hurt the DDA performance.

The qualitative verification showed the vorticity constraint DDA performed poorly when the verification column was close to a data void and the vorticity constraint could not be applied. Therefore, including these times and locations when
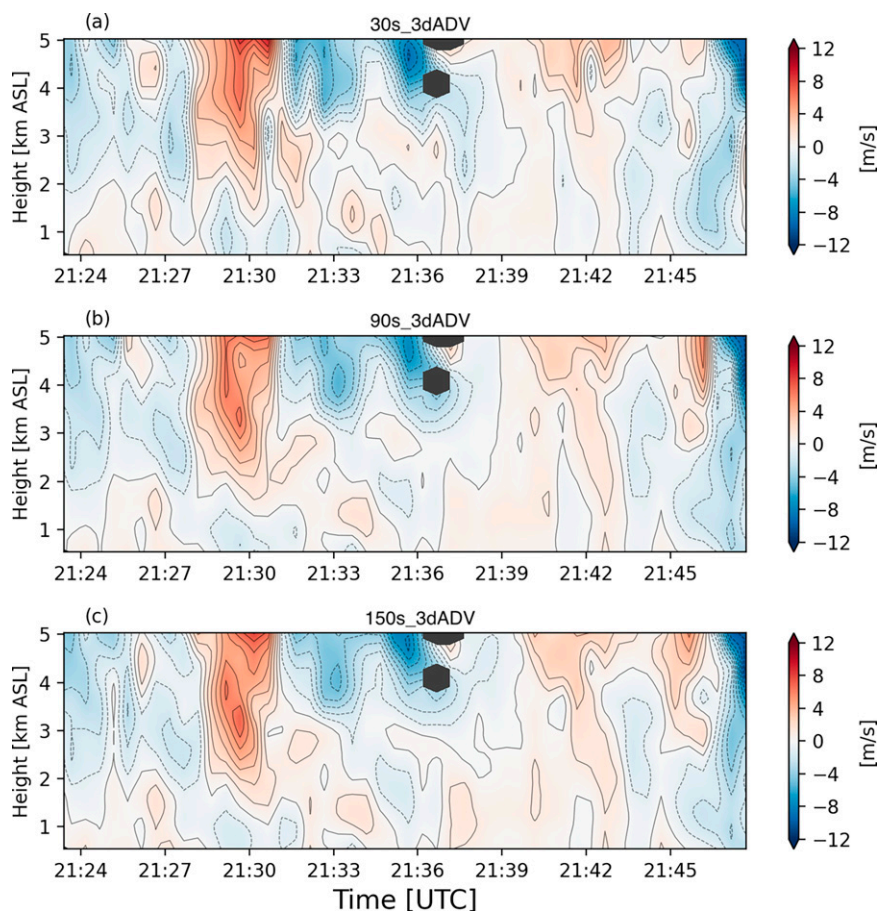
FIG. 7. As in Fig. 4, but for the (a) 30s_3DADV, (b) 90s_3DADV, and 150s_3DADV DDAs.

calculating the objective verification statistics may not represent the true skill of the vorticity constraint. If only the times and locations where the vorticity constraint is applied are used for the objective verification, the CRMSE is lower and the correlation coefficient increases for the vorticity constraint DDAs (Fig. 9). For the TRAD and NOVORT DDAs the CRMSE increases when the "no vorticity constraint points" are excluded. This suggests the improvements in CRMSE and correlation coefficient in the vorticity constraint DDAs are not merely due to the change in the sample of the verification points used for the calculation. While not shown in the present manuscript, these DDA verification results were similar when the DDAs were performed at 250-m resolution.

c. Domainwide KTLX verification

The SR1-P observations were the only observations of vertical velocity that could be used to verify the DDA vertical velocities, but the KTLX radial velocities can be used to assess DDA skill across the entire domain. Since KTLX scans with low elevations angles and was directly east of the storm, this verification mostly represents the DDAs' skill in retrieving u component of the wind. This verification is useful for quantifying differences in the horizontal winds between the

retrievals and ensuring the vorticity constraint is not degrading the horizontal winds. The KTLX radial velocities were gridded at the same horizontal resolution as the DDAs, but on conical surfaces for each KTLX sweep using a Cressman filter with a 1-km Cressman radius. Each sweep was gridded separately due to the longer scan times of KTLX. For each KTLX sweep, the radial velocities that would be observed by KTLX for the DDA wind field at the time closest to the KTLX sweep time were calculated. The RMSE between the KTLX-observed radial velocities and the calculated radial velocities from the DDA retrievals was determined for the entire DDA time period for each DDA experiment.

All experiments had a radial velocity RMSE between 2.085 and 2.172 m s^{-1} (Table 2). These minimal differences are expected and consistent with the Potvin et al. (2012b) OSSE results, as the horizontal wind field is not strongly affected by including a vorticity constraint since the horizontal winds are well constrained by observations.

d. Domainwide analysis of retrieved vertical velocity

Though there is no verification source for w across the domain, it is useful to compare the w field between the different DDA experiments. One feature that is very apparent in
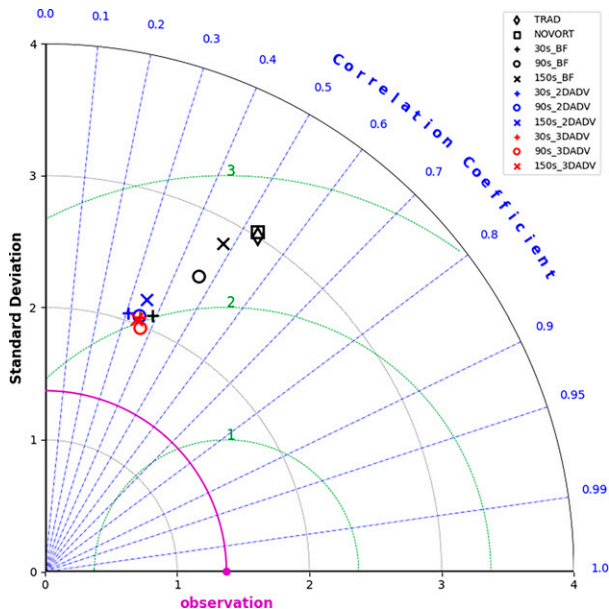
FIG. 8. Taylor diagram for the DDA experiments. Correlation coefficient is the angular coordinate, standard deviation (m s^{-1}) is the range coordinate, and CRMSE (m s^{-1}) is represented by the green contours. The observation standard deviation is shown with the magenta arc. The markers for the TRAD and NOVORT DDAs are a black diamond and square, respectively. The 30-s DDAs are represented by a cross, 90-s DDA by a circle, and 150-s DDAs by an ×. The technique for calculating the vorticity tendency is represented by color, with black markers for the brute force DDAs, blue markers for the 2D advection correction DDAs, and red markers for the 3D advection correction DDAs.

comparison is vorticity constraint DDAs have more spatial variability in w than the TRAD and NOVORT DDAs (Fig. 10). The tilting term in the vorticity equation explains this. Because horizontal gradients in w are present in that term, creating gradients in w is one way to balance the vorticity tendency.

Another feature that stands out is an excessively strong downdraft retrieved in the TRAD and NOVORT DDAs around 2130 UTC in the southwest region of the storm (Figs. 10a–d). The peak velocity of this downdraft is 48.84 m s^{-1} in the NOVORT DDA and 51.44 m s^{-1} in the TRAD DDA. These values are unrealistic for the environment that the storm developed in and are likely the result of a radar data observation error. After review, it was found that the RaXPol data likely had sidelobe contamination in this region of the storm that artificially enhanced divergence. This error, however, was serendipitous, revealing another advantage of the vorticity constraint DDA. The vorticity constraint DDAs did not produce the excessive downdraft seen in the TRAD and NOVORT DDAs (Figs. 10e,f). This indicates that the vorticity constraint may help to reduce w retrieval error when observation errors are present. As this study demonstrates, even with extensive quality control, radar data errors can remain in a dataset. This feature of using a vorticity constraint would be difficult to discover in an OSSE framework.
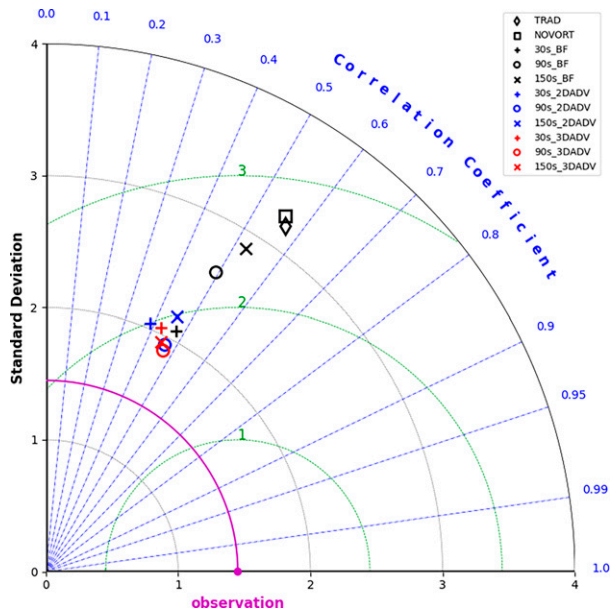

FIG. 9. As in Fig. 8, but only for the times and locations that have the vorticity constraint applied.

e. Comparing vorticity tendency calculations

The accuracy of the vorticity tendency calculation is critical for accurate vertical velocity retrievals using the vorticity constraint DDA. Analysis of the vorticity tendency estimates using the different techniques described in section 3a(3) can provide insights into the significant skill difference in the w retrievals. At the verification column, the 90s_BF and 150s_BF DDAs have lower estimates of the vorticity tendency magnitude than the other methods, and the magnitudes of the vorticity tendency in these DDAs are more constant throughout the entire period (Fig. 11). The 30s_BF DDAs have magnitudes of the vorticity tendency similar to those obtained in the advection correction DDAs, which suggest that 30-s volume scans are rapid enough to use the brute force technique for this dataset. The 90s_BF and 150s_BF vorticity tendencies significantly deviate from the magnitudes of the vorticity tendency of other techniques between 2130 and 2133 UTC and

TABLE 2. Radial velocity RMSE (m s^{-1}) from the KTLX observations for all DDA experiments.

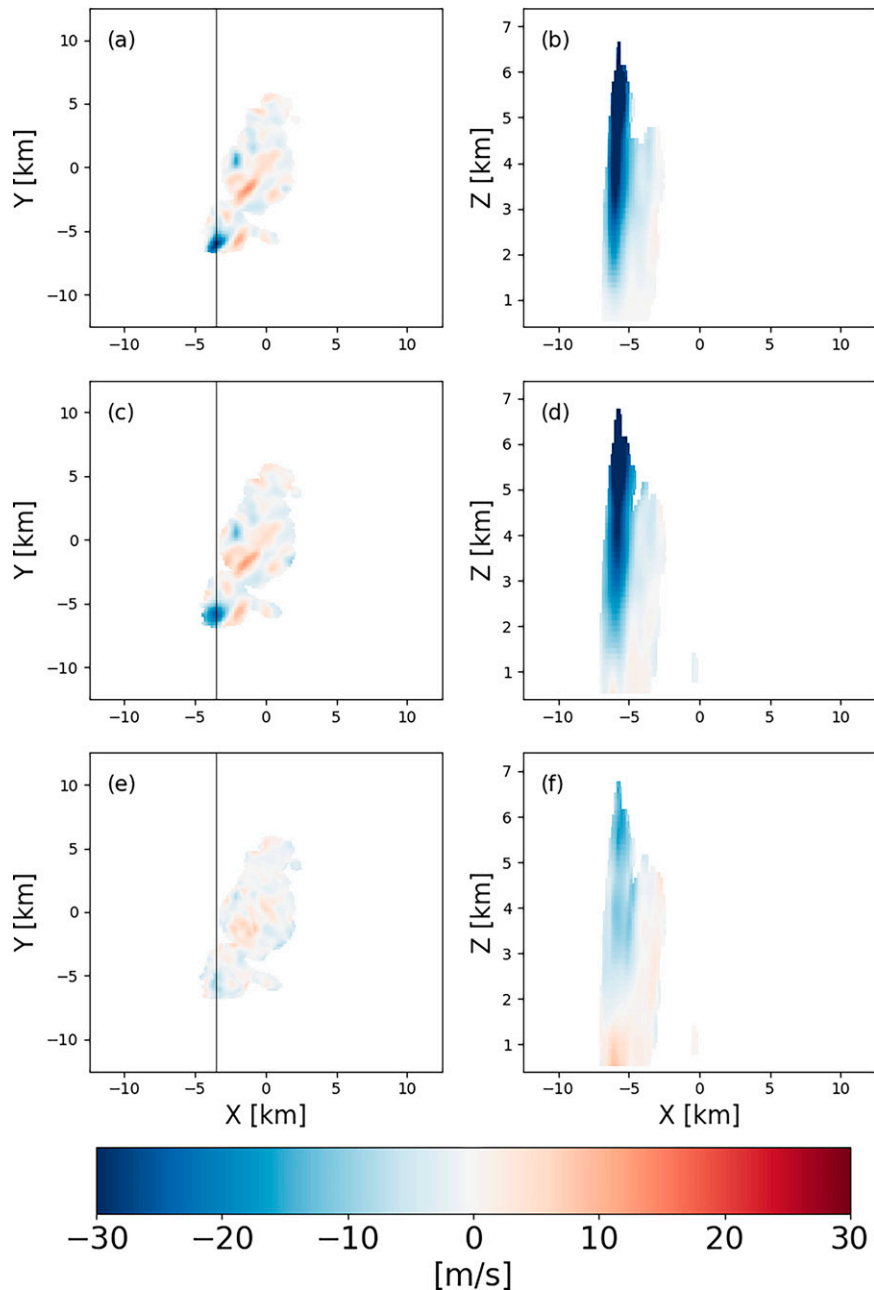| Expt	RMSE
TRAD	2.172
NOVORT	2.163
30s_BF	2.107
90s_BF	2.085
150s_BF	2.091
30s_2dADV	2.136
90s_2dADV	2.126
150s_2dADV	2.119
30s_3dADV	2.135
90s_3dADV	2.123
150s_3dADV	2.124

FIG. 10. (left) Retrieved vertical velocity at 2130:10 UTC from the (a) TRAD, (c) NOVORT, and (e) 90s_VORT_3DADV DDAs at 3.03 km MSL and (right) horizontal cross sections of retrieved vertical velocity at $x = -3.5$ km for the (b) TRAD, (d) NOVORT, and (f) 90s_VORT_3-DADV DDAs. The black line in (a), (c), and (e) shows the location of the cross section for (b), (d), and (f).

after 2145 UTC. These time periods are also when these DDAs produce their most inaccurate vertical velocity retrievals, with errors exceeded those in the TRAD and NOVORT DDAs.

Profiles of the vorticity tendency at 2131:40 UTC at the verification column change little with height in the 90s_BF and 150s_BF experiments while the other methods show much larger vertical variations (Fig. 12). The largest spread in the

vorticity tendency occurs above 3.5 km. The 150s_2DADV appears to underestimate the magnitude of the vorticity tendency above 3.5 km, and at this time this DDA produces an excessively strong updraft at the verification column. It is encouraging that the advection correction methods for calculating the vorticity tendency produced tendencies similar to the 30s_BF when volume scan times were 90 and 150 s. This
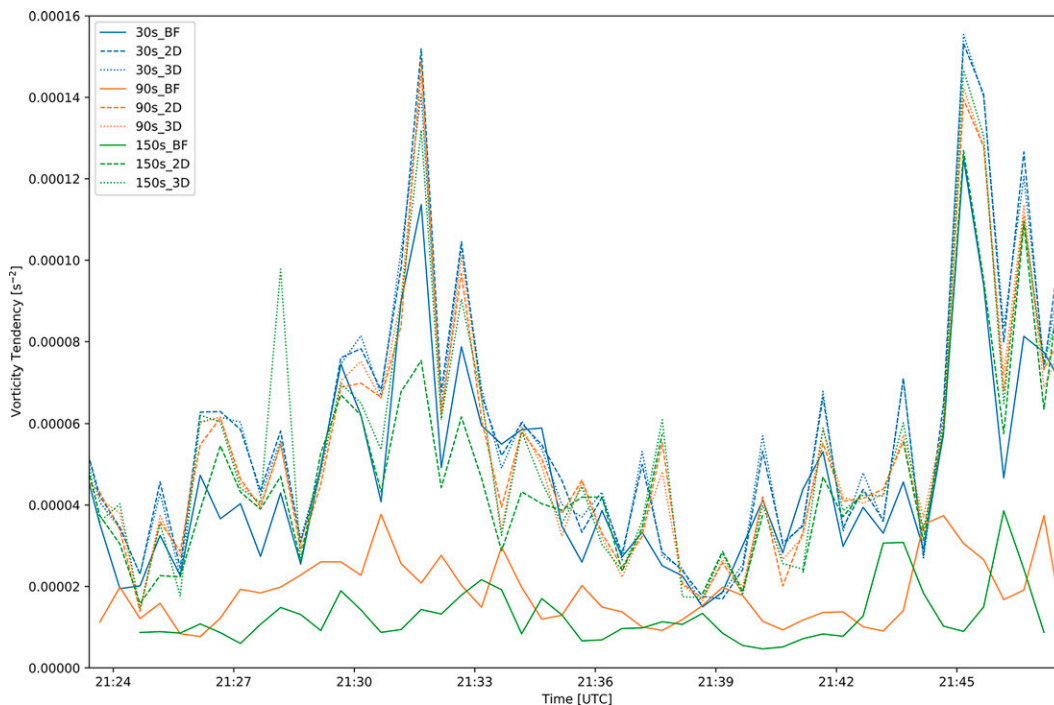
FIG. 11. Average magnitude of the vorticity tendency at the SR1-P verification column.

indicates that these techniques may enable the vorticity constraint DDA to be applied to datasets with slower volume scans rates than those suggested by Dahl et al. (2019). Of course, this was not a complex storm; these results may not hold for a storm with a stronger and more variable wind field.

5. Summary

The results of this study suggest a vertical vorticity equation constraint DDA can improve vertical velocity retrievals under the right conditions. This is consistent with prior OSSEs (Potvin et al. 2012b; Dahl et al. 2019), though the improvements in OSSE studies occurred in situations with substantial depths of missing low-level data. In this real-data test there was not a large data gap between the lowest level of data availability and the ground, indicating the vertical vorticity equation constraint can provide value even in the best data availability scenarios. This is likely due in part to the vorticity constraint DDA being more forgiving to observational errors. On the other hand, the vorticity constraint DDA is prone to large errors close to data voids where the vorticity tendency cannot be estimated. Therefore, caution should be used when interpreting results close to data voids, and it may be prudent to exclude these regions from the final analysis.

The time between volume scans had a significant impact on vertical velocity retrievals when basic centered differencing (brute force technique) was used for calculating the vorticity tendency. Compared with the TRAD and NOVORT DDAs, the brute force technique produced more accurate w retrievals with volume scans 30 s apart but resulted in larger errors with volume scans 90 or 150 s apart. Using an advection correction

method to calculate the vorticity tendency with volume scans 90 or 150 s apart yielded vorticity tendency estimates closer to those produced by the 30 s brute force method, substantially improving the w retrievals for those scan rates. Generally, using 3D advection correction produced slightly better results than using 2D advection correction, although this improvement was much less than the improvement of 2D advection correction over brute force estimation for longer scan times. The 30-s volume scan DDAs did not improve when using advection correction, potentially because there was not much possible improvement in the vorticity tendency estimate from the brute force estimates. The vorticity constraint DDAs appeared to be less sensitive to radar data errors than DDAs that did not impose a vorticity equation constraint. Sidelobe contamination in the radar dataset caused the TRAD and NOVORT DDAs to produce unrealistic downdrafts while the vorticity constraint DDAs did not. This new finding highlights why OSSE study results should always by followed be real-data tests, as this feature would be difficult to identify in an OSSE.

Finally, while the results of this study provide further support for including the vertical vorticity constraint in DDA, this is the first study to test the procedure with real, rapid-scan radar data. This study was limited to verifying low-level vertical velocity from the DDAs and future real-data studies will need to address how the vertical vorticity constraint DDAs perform at higher altitudes where vertical velocities are typically most intense. Additionally, future real-data tests should be conducted with different storm types and environments to see how well this studies' results generalize. This is particularly important for determining the volume scan time needed for accurate retrievals as
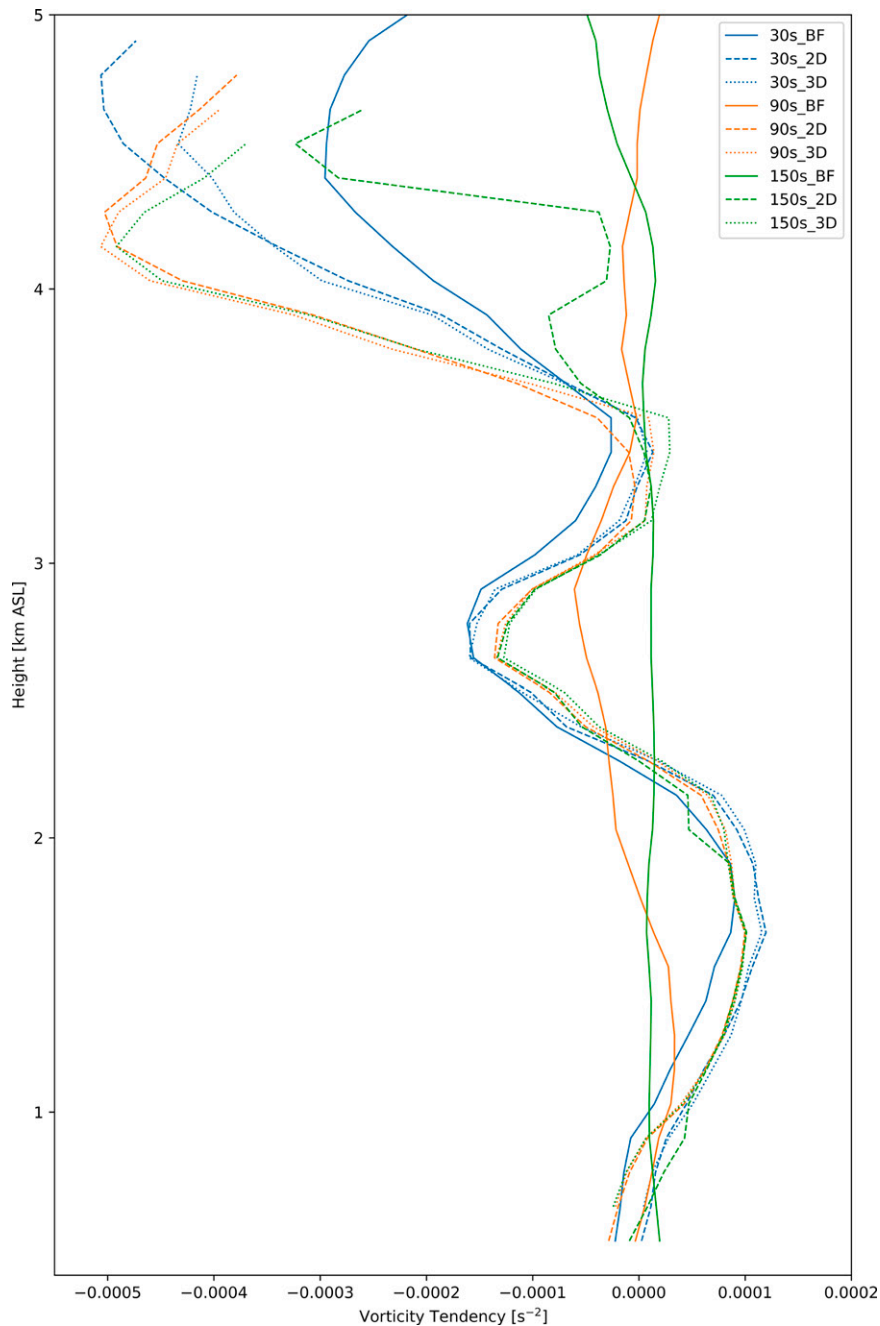
FIG. 12. Profiles of the calculated vorticity tendency at the SR1-P verification column for 2131:40 UTC DDAs.

different storms types may generate vorticity at varying time scales. The skill of the vorticity constraint DDA could also be dependent on the vertical wind shear present in the environment, as this impacts vertical vorticity generation due to tilting. Overall, the vorticity constraint DDA is a promising technique that is well suited to leverage the proliferation of rapid-scan radars.
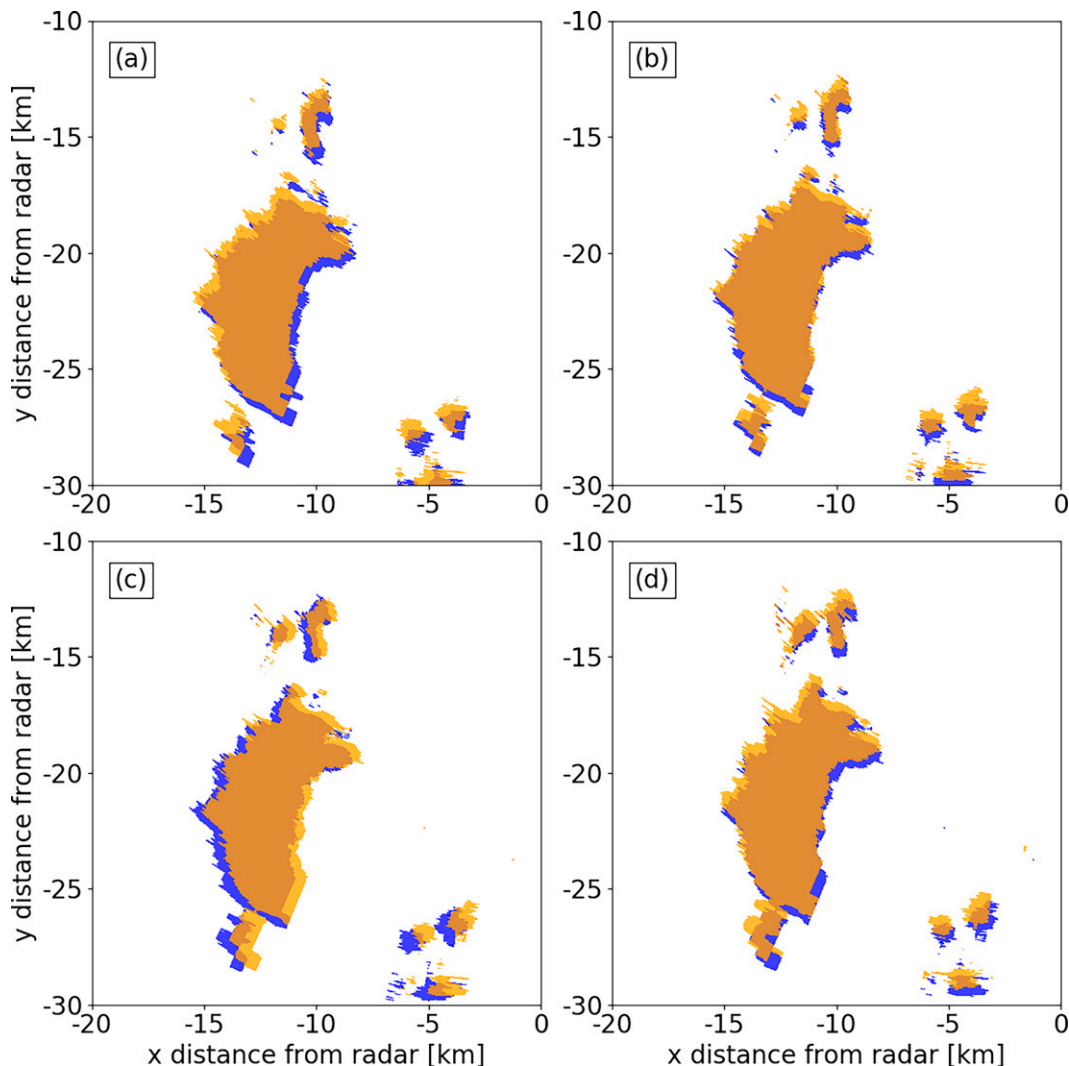
FIG. A1. Azimuthal displacements evident in the RaXPol data in consecutive scans. Areas with reflectivity greater than 25 dBZ at (a) 2112:11 (blue) and 2112:41 (orange), (b) 2112:41 (blue) and 2113:11 (orange), (c) 2113:11 (blue) and 2113:41 (orange), and (d) 2113:41 (blue) and 2114:11 UTC (orange) from the 1° RaXPol PPI scans.

made to incorporate the techniques described in this study into PyDDA (github.com/openradar/PyDDA). The advection correction code used in this study is available at github.com/jgebauer44/ADV_Cor.

APPENDIX

Correction of Spatially Variable Azimuthal Displacement Errors

Correcting for azimuthal displacement errors is somewhat common with mobile radar datasets and can even be necessary with fixed-position radars. Some azimuthal displacement errors can be corrected using ground clutter (Rico-Ramirez et al. 2009) or the radiation emitted by the sun (Arnott et al. 2003; Muth et al. 2012). However, the unique aspects of the azimuthal displacements in

the 4 September 2018 RaXPol dataset required a new technique.

Azimuthal displacement errors that vary between scans will cause apparent perturbations in the azimuthal velocity of a radar echo in a polar coordinate system centered on the radar. If the true azimuthal advection speed is known (even coarsely) and the deviations from the that speed—which are largely due to the erroneous azimuthal shifts—can be determined, the azimuthal displacements can potentially be corrected. This is the premise of the azimuthal displacement correction technique developed for the RaXPol dataset.

The radar echo's azimuthal velocities are calculated from the Cartesian pattern translation velocities retrieved by the Shapiro et al. (2010) spatially variable advection correction routine. This technique requires the input data to be on a Cartesian grid, so a Cressman filter (Cressman 1959) with a 400-m Cressman radius was used to put the
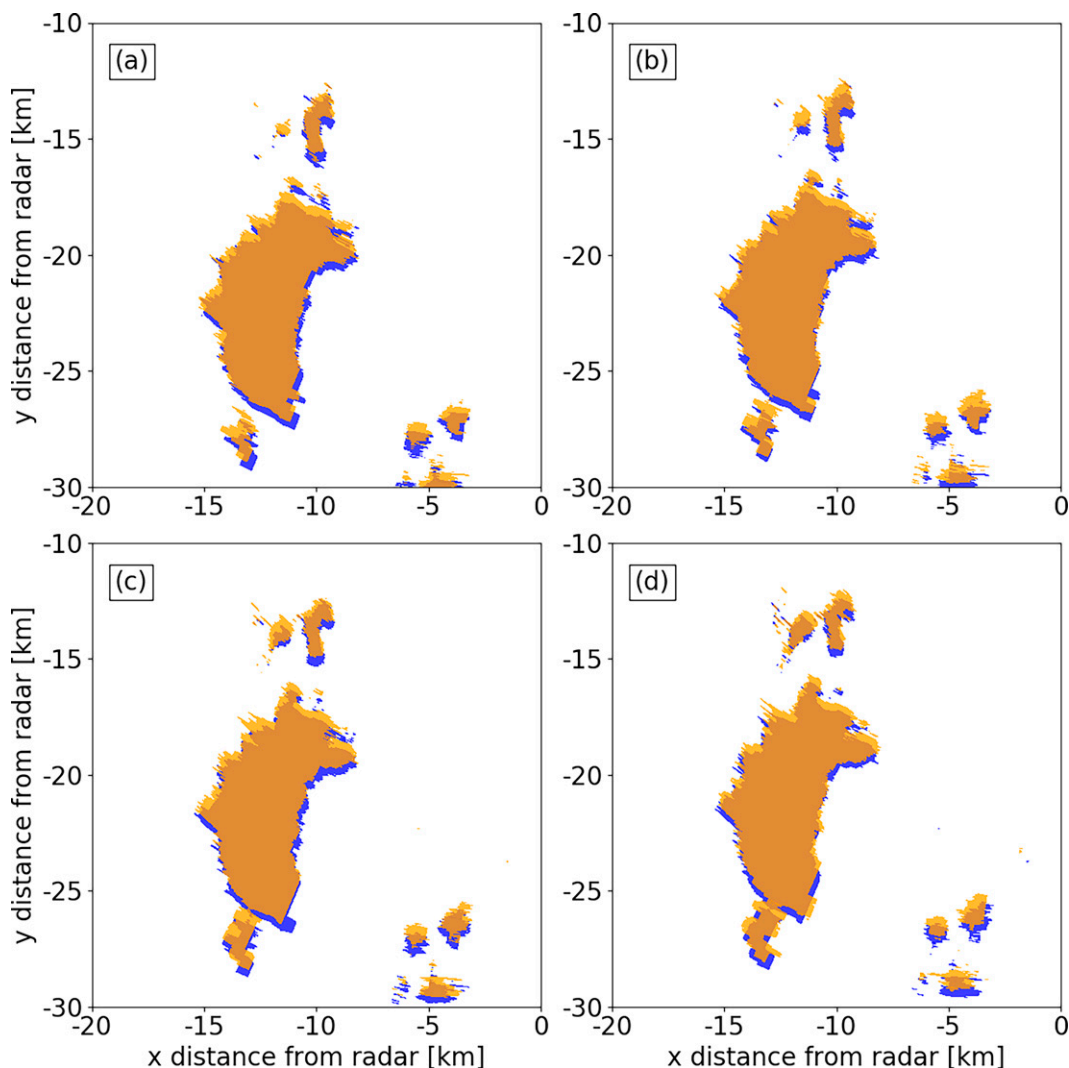
FIG. A2. Areas with reflectivity greater than 25 dBZ for same scans as in Fig. A1, but after the azimuthal displacement correction.

data from every PPI scan on a 125-m grid. Then, for each elevation angle, the pattern translation components between consecutive scans were found for the entire RaXPol data collection period using the Shapiro et al. (2010) procedure. The true pattern translation components are not known; however, the randomness of the displacement errors suggests that the mean pattern translation components from a large number of sweeps should lead to a reasonably accurate estimate of the pattern translation components. For the 4 September 2018 RaXPol dataset, the pattern translation is roughly uniform in both time and space, so the pattern translation components for the entire data collection period is used to calculate the mean. For a more complex storm environment with variable storm motion, smaller averaging windows would need to be used.

Once the Cartesian pattern translation components are retrieved, they are converted to the radial and azimuthal

pattern translation components for the polar coordinate system centered on the radar. The perturbation azimuthal velocity is calculated by subtracting the local azimuthal velocity computed from the mean pattern translation components from the local azimuthal velocity of each sweep. From these perturbation azimuthal velocities, the displacements can be calculated by first calculating perturbation angular velocity and then multiplying the perturbation angular velocity by the time between volume scans. The last step before correcting the displacements is to calculate a 15° azimuthal mean of the displacements centered on each azimuth in the sweep. The 15° mean displacements are used for the final correction to prevent large distortions in the spacing between azimuths.

The correction of the displacements starts with the second sweep for each elevation scan and proceeds sequentially. If the previous sweep's displacement for a particular azimuth was of the opposite sign, the previous sweep's

correction is subtracted from the current sweep's correction to account for the calculated displacement actually representing the data shifting back to their correct position. This prevents overcorrection. Then, for the next sweep, the sign of the previous displacement does not matter for the correction since the displacement should be a shift from the true location. The procedure continues until all sweeps are corrected.

This correction technique reduces but does not completely eliminate the displacements errors (Figs. A1, A2). The success of the displacement correction is largely dependent on the accuracy of the pattern translation components retrieved from the advection correction procedure. Inaccurate advection correction results can occur due to solution nonuniqueness, or due to small gradients in the reflectivity in the direction of the pattern translation vectors. Additionally, since each elevation scan was corrected independently, the quality of the correction can vary for each elevation scan in a volume. Overall, this technique is most successful at reducing the largest displacements where the precision of the advection correction technique is less important. The technique shows promise with this dataset though, the advection speeds appeared to be largely independent of height and location based on inspection of the reflectivity imagery. It is unknown if the correction will be as successful for more complex datasets.

REFERENCES

Alford, A. A., M. I. Biggerstaff, and G. D. Carrie, 2019: Mobile ground-based smart radar observations and wind retrievals during the landfall of Hurricane Harvey (2017). *Geosci. Data J.*, **6**, 205–213, https://doi.org/10.1002/gdj3.82.

Arnott, N. R., Y. P. Richardson, J. M. Wurman, and J. Lutz, 2003: A solar alignment technique for determining mobile radar pointing angles. *31st Int. Conf. on Radar Meteorology*, Amer. Meteor. Soc, Seattle, WA, P3C.12, https://ams.confex.com/ams/32BC31R5C/techprogram/paper_64336.htm.

Atlas, D., R. C. Srivastava, and R. S. Sekhon, 1973: Doppler radar characteristics of precipitation at vertical incidence. *Rev. Geophys. Space Phys.*, **11**, 1–35, https://doi.org/10.1029/RG011i001p00001.

Betten, D. P., M. I. Biggerstaff, and C. L. Ziegler, 2018: Three-dimensional storm structure and low-level boundaries at different stages of cyclic mesocyclone evolution in a high-precipitation tornadic supercell. *Adv. Meteor.*, **2018**, 9432670, https://doi.org/10.1155/2018/9432670.

Biggerstaff, M. I., and R. A. Houze Jr., 1993: Kinematics and microphysics of the transition zone of the 10–11 June 1985 squall line. *J. Atmos. Sci.*, **50**, 3091–3110, https://doi.org/10.1175/1520-0469(1993)050<3091:KAMOTT>2.0.CO;2.

——, and Coauthors, 2005: The Shared Mobile Atmospheric Research and Teaching radar: A collaboration to enhance research and teaching. *Bull. Amer. Meteor. Soc.*, **86**, 1263–1274, https://doi.org/10.1175/BAMS-86-9-1263.

Brandes, E. A., 1977: Flow in severe thunderstorms observed by dual-Doppler radar. *Mon. Wea. Rev.*, **105**, 113–120, https://doi.org/10.1175/1520-0493(1977)105<0113:FISTOB>2.0.CO;2.

——, R. P. Davies-Jones, and B. C. Johnson, 1988: Streamwise vorticity effects on supercell morphology and persistence.

J. Atmos. Sci., **45**, 947–963, https://doi.org/10.1175/1520-0469(1988)045<0947:SVEOSM>2.0.CO;2.

Conrad, D. M., and K. R. Knupp, 2019: Doppler radar observations of horizontal shearing instability in quasi-linear convective systems. *Mon. Wea. Rev.*, **147**, 1297–1318, https://doi.org/10.1175/MWR-D-18-0257.1.

Cressman, G. P., 1959: An operational objective analysis system. *Mon. Wea. Rev.*, **87**, 367–374, https://doi.org/10.1175/1520-0493(1959)087<0367:AOOAS>2.0.CO;2.

Crum, T. D., and R. L. Alberty, 1993: The WSR-88D and the WSR-88D Operational Support Facility. *Bull. Amer. Meteor. Soc.*, **74**, 1669–1687, https://doi.org/10.1175/1520-0477(1993)074<1669:TWATWO>2.0.CO;2.

——, R. E. Saffle, and J. W. Wilson, 1998: An update on the NEXRAD program and future WSR-88D support to operations. *Wea. Forecasting*, **13**, 253–262, https://doi.org/10.1175/1520-0434(1998)013<0253:AUOTNP>2.0.CO;2.

Dahl, N. A., A. Shapiro, C. K. Potvin, A. Theisen, J. G. Gebauer, A. D. Schenkman, and M. Xue, 2019: High-resolution, rapid-scan dual-Doppler retrievals of vertical velocity in a simulated supercell. *J. Atmos. Oceanic Technol.*, **36**, 1477–1500, https://doi.org/10.1175/JTECH-D-18-0211.1.

Doviak, R. J., P. S. Ray, R. G. Strauch, and L. J. Miller, 1976: Error estimation in wind fields derived from dual-Doppler radar measurement. *J. Atmos. Oceanic Technol.*, **15**, 868–878, https://doi.org/10.1175/1520-0450(1976)015<0868:EEIWFD>2.0.CO;2.

Gao, J., M. Xue, A. Shapiro, and K. K. Droegemeier, 1999: A variational method for the analysis of three-dimensional wind fields from two Doppler radars. *Mon. Wea. Rev.*, **127**, 2128–2142, https://doi.org/10.1175/1520-0493(1999)127<2128:AVMFTA>2.0.CO;2.

Gebauer, J. G., 2020: Assessing dual-Doppler vertical velocity retrievals from rapid-scan radar data. Ph.D. dissertation, University of Oklahoma, 158 pp.

Isom, B., and Coauthors, 2013: The Atmospheric Imaging Radar: Simultaneous volumetric observations using a phased array weather radar. *J. Atmos. Oceanic Technol.*, **30**, 655–675, https://doi.org/10.1175/JTECH-D-12-00063.1.

Kosiba, K. A., and J. Wurman, 2014: Finescale dual-Doppler analysis of hurricane boundary layer structures in Hurricane Frances (2004) at landfall. *Mon. Wea. Rev.*, **142**, 1874–1891, https://doi.org/10.1175/MWR-D-13-00178.1.

——, ——, Y. Richardson, P. Markowski, P. Robinson, and J. Marquis, 2013: Genesis of the Goshen County, Wyoming, tornado on 5 June 2009 during VORTEX2. *Mon. Wea. Rev.*, **141**, 1157–1181, https://doi.org/10.1175/MWR-D-12-00056.1.

Kurdzo, J. M., and Coauthors, 2017: Observations of severe local storms and tornadoes with the Atmospheric Imaging Radar. *Bull. Amer. Meteor. Soc.*, **98**, 915–935, https://doi.org/10.1175/BAMS-D-15-00266.1.

Lang, T. J., and S. A. Rutledge, 2002: Relationships between convective storm kinematics, precipitation, and lightning. *Mon. Wea. Rev.*, **130**, 2492–2506, https://doi.org/10.1175/1520-0493(2002)130<2492:RBCSKP>2.0.CO;2.

Leise, J. A., 1982: A multidimensional scale-telescoped filter and data extension package. NOAA Tech. Memo. ERL WPL-82, 19 pp.

Mahoney, W. P., 1988: Gust front characteristics and the kinematics associated with interacting thunderstorm outflows. *Mon. Wea. Rev.*, **116**, 1474–1492, https://doi.org/10.1175/1520-0493(1988)116<1474:GFCATK>2.0.CO;2.

Matejka, T., and D. L. Bartels, 1998: The accuracy of vertical air velocities from Doppler radar data. *Mon. Wea. Rev.*,

126, 92–117, https://doi.org/10.1175/1520-0493(1998)126<0092:TAOVAV>2.0.CO;2.

Muth, X., M. Schneebeli, and A. Berne, 2012: A sun-tracking method to improve the pointing accuracy of weather radar. *Atmos. Meas. Tech.*, **5**, 547–555, https://doi.org/10.5194/amt-5-547-2012.

Nelson, S. P., and R. A. Brown, 1987: Error sources and accuracy of vertical velocities computed from multiple-Doppler radar measurements in deep convective storms. *J. Atmos. Oceanic Technol.*, **4**, 233–238, https://doi.org/10.1175/1520-0426(1987)004<0233:ESAAOV>2.0.CO;2.

O'Brien, J. J., 1970: Alternative solutions to the classical vertical velocity problem. *J. Appl. Meteor.*, **9**, 197–203, https://doi.org/10.1175/1520-0450(1970)009<0197:ASTTCV>2.0.CO;2.

Oye, R. C., C. Mueller, and S. Smith, 1995: Software for radar translation, visualization, editing, and interpolation. *27th Conf. on Radar Meteorology*, Amer. Meteor. Soc, Vail, CO, 359–361.

Pazmany, A., J. Mead, H. Bluestein, J. Snyder, and J. Houser, 2013: A mobile rapid-scanning X-band polarimetric (RaXPol) Doppler radar system. *J. Atmos. Oceanic Technol.*, **30**, 1398–1413, https://doi.org/10.1175/JTECH-D-12-00166.1.

Potvin, C. K., D. Betten, L. J. Wicker, K. L. Elmore, and M. I. Biggerstaff, 2012a: 3DVAR versus traditional dual-Doppler wind retrievals of a simulated supercell thunderstorm. *Mon. Wea. Rev.*, **140**, 3487–3494, https://doi.org/10.1175/MWR-D-12-00063.1.

——, A. Shapiro, and M. Xue, 2012b: Impact of a vertical vorticity constraint in variational dual-Doppler wind analysis: Tests with real and simulated supercell data. *J. Atmos. Oceanic Technol.*, **29**, 32–49, https://doi.org/10.1175/JTECH-D-11-00019.1.

Protat, A., and I. Zawadzki, 1999: A variational method for real-time retrieval of three-dimensional wind field from multiple-Doppler bistatic radar network data. *J. Atmos. Oceanic Technol.*, **16**, 432–449, https://doi.org/10.1175/1520-0426(1999)016<0432:AVMFRT>2.0.CO;2.

Ray, P. S., and K. K. Wagner, 1976: Multiple Doppler radar observations of storms. *Geophys. Res. Lett.*, **3**, 189–191, https://doi.org/10.1029/GL003i003p00189.

——, C. L. Ziegler, W. Bumgarner, and R. J. Serafin, 1980: Single- and multiple-Doppler radar observations of tornadic storms. *Mon. Wea. Rev.*, **108**, 1607–1625, https://doi.org/10.1175/1520-0493(1980)108<1607:SAMDRO>2.0.CO;2.

Rico-Ramirez, M., E. Gonzalez-Ramirez, I. Cluckie, and D. Han, 2009: Real-time monitoring of weather radar antenna pointing using digital terrain elevation and a Bayes clutter classifier. *Meteor. Appl.*, **16**, 227–236, https://doi.org/10.1002/met.112.

Sasaki, Y., 1970: Some basic formalisms in numerical variational analysis. *Mon. Wea. Rev.*, **98**, 875–883, https://doi.org/10.1175/1520-0493(1970)098<0875:SBFINV>2.3.CO;2.

Shapiro, A., C. K. Potvin, and J. Gao, 2009: Use of a vertical vorticity equation in variational dual-Doppler wind analysis. *J. Atmos. Oceanic Technol.*, **26**, 2089–2106, https://doi.org/10.1175/2009JTECHA1256.1.

——, K. M. Willingham, and C. K. Potvin, 2010: Spatially variable advection correction of radar data. Part II: Test results. *J. Atmos. Sci.*, **67**, 3457–3470, https://doi.org/10.1175/2010JAS3466.1.

Taylor, K. E., 2001: Summarizing multiple aspects of model performance in a single diagram. *J. Geophys. Res.*, **106**, 7183–7192, https://doi.org/10.1029/2000JD900719.